Journal of
Asian Earth Sciences

Postseismic deformation following the 2 July 2013 M_w 6.1 Aceh, Indonesia, earthquake estimated using GPS data

Endra Gunawan, Sri Widiyantoro, Zulfakriza,
Irwan Meilano, Cecep Pratama

Journal of Asian Earth Sciences 177 (2019) 146–151

Contents lists available at ScienceDirect

Journal of Asian Earth Sciences

journal homepage: www.elsevier.com/locate/jseaes

Full length article

Postseismic deformation following the 2 July 2013 M_w 6.1 Aceh, Indonesia, earthquake estimated using GPS data

Endra Gunawan[a,*], Sri Widiyantoro[a], Zulfakriza[a], Irwan Meilano[b], Cecep Pratama[c]

[a] Global Geophysics Research Group, Faculty of Mining and Petroleum Engineering, Bandung Institute of Technology, Indonesia
[b] Geodesy Research Group, Faculty of Earth Science and Technology, Bandung Institute of Technology, Indonesia
[c] Department of Geodetic Engineering, Gadjah Mada University, Indonesia

ARTICLE INFO

Keywords:
2 July 2013 Aceh earthquake
GPS
Postseismic deformation
Poroelastic rebound
Viscoelastic relaxation
Afterslip

ABSTRACT

GPS data after the 2 July 2013 M_w 6.1 Aceh earthquake provide valuable information for understanding the postseismic behavior of a strike-slip fault in northern Sumatra, Indonesia. The analysis of postseismic deformation following the 2004 Sumatra-Andaman earthquake and the 2012 Indian Ocean earthquake suggest that the ongoing deformation affected northern Sumatra between July and December 2013. The postseismic deformation of the 2013 Aceh earthquake is herein investigated, with the contribution of poroelastic rebound and viscoelastic relaxation evaluated. The results suggest that the model displacement of those two mechanisms failed to estimate the data. The afterslip analysis of the 2013 Aceh earthquake, on the contrary, fits the data very well with a seismic slip occurring at multiple fault segments of the Sumatran fault in northern Sumatra, Indonesia.

1. Introduction

The devastating 2 July 2013 M_w 6.1 Aceh earthquake (AE) occurred along a newly identified active left-lateral fault segment of the Sumatran fault in northern Sumatra, Indonesia, identified as the Celala segment (Gunawan et al., 2018). A previous study suggested that the 2 July 2013 earthquake occurred as the Celala segment was 0.1 MPa closer to failure after the earlier 21 January 2013 M_w 6.1 AE (Ito et al., 2016). Prior to the event, the Celala segment was unmapped and unidentified. As a result of this unexpected earthquake event, losses were high. The Indonesian National Board for Disaster Management (2013) reported casualties of 43 people dead and six others missing, with economic losses of more than US$ 50 million; another US$ 70 million was needed for rehabilitation and reconstruction after the disaster. Fig. 1 shows the tectonic setting of this region.

Modern geodetic tools such as GPS have been widely used to understand the crustal deformation of the earthquake cycle, corresponding to interseismic, coseismic, and postseismic deformation (e.g. Wang et al., 2012). Previous studies propose postseismic deformation mechanisms after earthquake occurrences, including poroelastic rebound, afterslip, and viscoelastic relaxation (e.g. Freed, 2007; Pollitz et al., 2012). One of the major differences between these mechanisms is the time duration. While poroelastic rebound is in days or weeks, afterslip could take months or years, and viscoelastic relaxation lasts for years or decades (Jónsson et al., 2003; Miyazaki et al., 2004; Lorenzo-Martín et al., 2006).

This study analyzes the postseismic deformation of the 2 July 2013 AE by considering these three postseismic deformation mechanisms. Unpublished GPS data available in the region are used for the analysis. The contributions of postseismic deformation after the 2004 M_w 9.2 Sumatra-Andaman earthquake (SAE) and the 2012 M_w 8.6 Indian Ocean earthquake (IOE) are considered in the analysis.

2. GPS observation and data processing

This study utilizes GPS data from campaign observations measured by the Bandung Institute of Technology on 15–18 July 2013 and 7–10 December 2013. The monumentation of the GPS stations comprised 30 cm steel pins cemented into bedrock. GPS campaign surveys were observed using L1/L2 geodetic-type receivers and GPS data were logged at a 30-s sampling rate. The locations of the GPS stations used in this study are in Fig. 1.

Daily solution analysis at each GPS station was performed using Bernese 5.2 (Dach et al., 2015). In our procedure, to estimate the daily solutions of GPS data, we first performed a Precise Point Positioning analysis. Ionosphere models and parameters for orbit-related satellites such as the parameters of Earth rotation, satellite clock coefficients, precise ephemerides, and differential code biases for a satellite and

* Corresponding author.
E-mail address: endra.gunawan@itb.ac.id (E. Gunawan).

https://doi.org/10.1016/j.jseaes.2019.03.020
Received 21 November 2018; Received in revised form 14 March 2019; Accepted 26 March 2019
Available online 27 March 2019

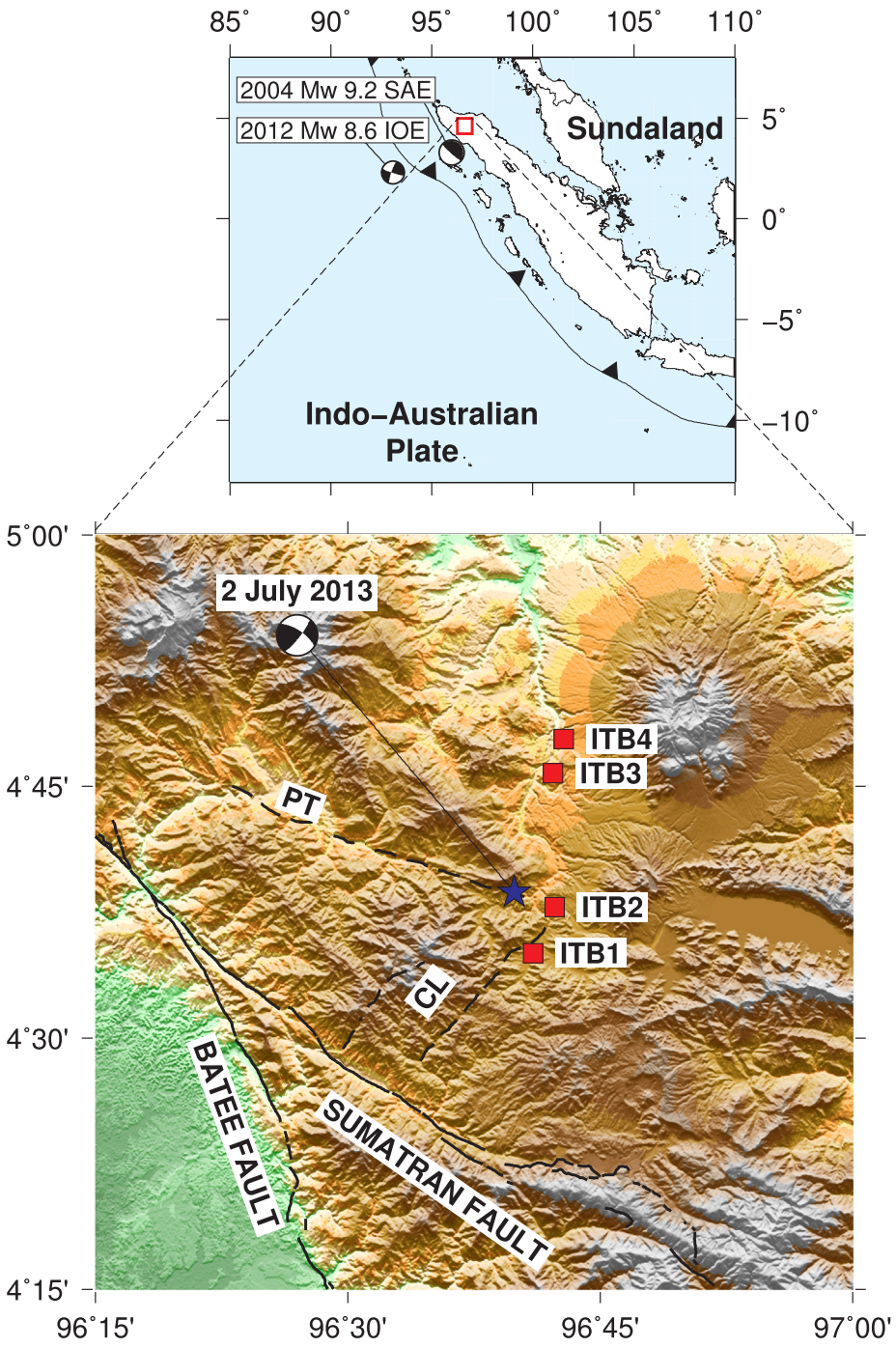

Fig. 1. Tectonic setting of this study. The blue star indicates the epicenter of the 2 July 2013 AE based on the United States Geological Survey catalog. The red squares indicate GPS stations, while the solid black lines suggest the locations of the identified Sumatran and Batee faults (Sieh and Natawidjaja, 2000). The dashed line marks the newly identified fault segments of Pantan Terong (PT) and Celala (CL). Topography created using Shuttle Radar Topography Mission (SRTM) 90 m (Jarvis et al., 2008). The inset shows the global map and the epicenter of the 2004 SAE and 2012 IOE. (For interpretation of the references to color in this figure legend, the reader is referred to the web version of this article.)

receivers were downloaded from the Astronomical Institute, University of Bern website (http://www.aiub.unibe.ch/). For station-related files such as ocean tidal loading, we employed Finite Element Solutions 2004 (Lyard et al., 2006), calculated from the website of the Onsala Space Observatory (http://holt.oso.chalmers.se/loading/). Meanwhile, atmospheric tidal loading for each GPS station was calculated at the Global Geophysical Fluids Center website (van Dam and Ray, 2010). Second, we used the required input parameters and a priori information from the first step to perform a double-difference, network-processing analysis, from which we obtained station coordinates with resolved ambiguity and minimum-constraint network solutions to the millimeter level of accuracy.

To help assess local deformation, site displacements were resolved to the Sundaland block reference frame. We used the Sundaland block parameters Simons et al. (2007) defined in the International Terrestrial Reference Frame (ITRF) 2000, with the rotation pole located at 49.0°N, −94.2°E and a clockwise rotation rate of 0.34°/Myr. Thus, coordinate transformation from ITRF2008 into ITRF2000 was done prior to the conversion into the Sundaland block reference frame (Altamimi et al., 2011).

Located ~300 km from the epicenter of the 2004 M_w 9.2 SAE, our study area was affected by postseismic deformation from this earthquake (Ito et al., 2012; Gunawan et al., 2014). Hence, the contribution of postseismic deformation from the 2004 SAE should be removed prior to analyzing the postseismic deformation of the 2 July 2013 AE. In addition, the occurrence of the 2012 M_w 8.6 IOE deforms Andaman-Nicobar, Sumatra, and Java, as detected by GPS data available in the region (Hill et al., 2015). While GPS data in Andaman-Nicobar detected

coseismic displacements of ~41 mm (Yadav et al., 2013), large displacements were observed in northern Sumatra at ~170 mm (Feng et al., 2015). To the south, a much lower magnitude of displacement of ~3 mm was observed by GPS stations in southern Sumatra and Java Island (Gunawan et al., 2016b).

The implication of the crustal deformation in northern Sumatra after those earthquakes occurrences for our GPS data can be defined as follows:

$$GPS = Postseismic_{2004\_SAE} + Postseismic_{2012\_IOE} + Postseismic_{2013\_AE} \quad (1)$$

3. Postseismic deformation of the 2004 SAE

In this study, we estimate two possible postseismic deformation mechanisms of the 2004 SAE that involved and affected our GPS data: afterslip and viscoelastic relaxation (e.g. Gunawan et al., 2016a). We rule out the possibility of poroelastic rebound, as it is unlikely that it emerged ~8.5 years after the 2004 SAE (e.g. Freed, 2007).

The viscoelastic relaxation of the 2004 SAE is calculated using the coseismic slip model of Rhie et al. (2007), which is estimated based on a joint inversion of seismic and geodetic data. In our rheology model, we use an elastic layer thickness of 65 km on top of the viscoelastic mantle defined by the Maxwell rheology with a viscosity (η_M) of 8.0×10^{18} Pa·s shallower than 220 km. From 220 to 670 km depth, we use a Maxwell viscosity (η_M) of 1.0×10^{20} Pa·s (Fig. 2; Gunawan et al., 2014). In our calculation using VISCO1D code (Pollitz, 1997), we find that the surface displacement at GPS stations generated by the viscoelastic relaxation of the 2004 SAE during July to December 2013 was ~10 mm.

For afterslip, the surface displacement is obtained by interpolating the afterslip moment estimated by the GPS data available from 2005 to 2009 (Gunawan et al., 2014). During July to December 2013, the afterslip moment is estimated at 9.8×10^{18} N·m (~M_w 6.6). Using this information, we estimate the surface displacements at GPS stations using an elastic half-space model (Okada, 1992). The results suggest that afterslip generated surface displacements of ~2 mm at our GPS stations. The cumulative surface displacements of afterslip and viscoelastic relaxation after the 2004 SAE are in Fig. 3.

4. Postseismic deformation of the 2012 IOE

Previous studies have suggested that the 2012 M_w 8.6 IOE occurred as a result of the stress transfer of the 2004 SAE and the 2005 Nias earthquake (Delescluse et al., 2012; Wiseman and Bürgmann, 2012). In this study, we estimate the viscoelastic relaxation of the 2012 IOE using PyLith 2.1.0 (Aagaard et al., 2013, 2015). In our model, we use previous study analysis by incorporating subducting slab into our model, with a 75 km thickness (Pratama et al., 2017).

Following Pratama et al. (2017), beneath the oceanic lithosphere up to 220 km depth, we use the Burgers body viscoelastic mantle with a Kelvin viscosity (η_K) of 1.0×10^{17} Pa·s and a Maxwell viscosity (η_M) of 2.0×10^{18} Pa·s. Meanwhile, for the continental asthenosphere, we employ a Maxwell viscosity (η_M) of 9.0×10^{18} Pa·s. At 220–670 km depth, we use a Maxwell viscosity (η_M) of 1.0×10^{20} Pa·s for both the oceanic and the continental region. Fig. 2 shows the rheology model of the 2012 IOE used in this study.

The afterslip of the 2012 IOE is estimated based on the stress distribution due to the coseismic stress change governed by the static friction law (Aagaard et al., 2013). Therefore, we combine the spatial distribution of the surface displacement resulting from afterslip at GPS stations with the modeled temporal decay of the logarithmic function. In that sense, the surface motion due to afterslip from the intended time periods exhibits total afterslip.

During July to December 2013, the surface displacements associated with the viscoelastic relaxation and afterslip of the 2012 IOE at GPS stations correspond to 5–8 mm and 1–2 mm, respectively. The cumulative model displacement from viscoelastic relaxation and afterslip is then 6–10 mm. Fig. 3 shows the modeled cumulative displacements of postseismic deformation after the 2012 IOE at GPS stations.

During investigating the postseismic deformation of the 2012 IOE, we avoided to use the model from Gunawan et al. (2014) for the 2012 IOE because their model is constructed for the 2004 SAE case, not the 2012 IOE. Likewise, the Pratama et al. (2017) investigated postseismic deformation of the 2012 IOE, and not the 2004 SAE. Thus, we follow those two studies for different earthquake cases, and used the information in our analysis.

5. Postseismic deformation of the 2013 AE

After removing the postseismic deformation of the 2004 SAE and 2012 IOE, GPS data residues are matched to the postseismic deformation of the 2 July 2013 AE. We then model these data residues by incorporating the postseismic deformation mechanisms—poroelastic rebound, viscoelastic relaxation, and afterslip—described below.

5.1. Poroelastic rebound

Poroelastic rebound has been proposed as a phenomenon associated with strike slip earthquake events (e.g. Jónsson et al., 2003). Resulting from pore pressure during an earthquake event, poroelastic rebound generates subsidence in the compressional coseismic region and uplift in the extensional coseismic region. Thus, the vertical component plays an important role in evaluating the contribution of poroelastic rebound to the data (Peltzer et al., 1998).

In our investigation, we model poroelastic rebound by subtracting coseismic dislocation from the elastic half-space model (Okada, 1992) of the undrained and drained values of Poisson's ratio. For the undrained Poisson's ratio, we use $\nu_u = 0.31$, while the drained value is $\nu_d = 0.27$, applying the same value of the shear modulus, that is 30 GPa, to both cases. Our analysis uses the coseismic slip distribution estimated based on GPS data (Fig. 4; Gunawan et al., 2018).

Our horizontal and vertical displacement model associated with poroelastic rebound is shown in Fig. 5. The horizontal component model shows very small magnitude displacements (< 0.2 mm) at these four GPS stations. Hence, in terms of the magnitude of horizontal displacements, the model fails to predict the data. Similarly, the displacement model of the vertical component shows subsidence where

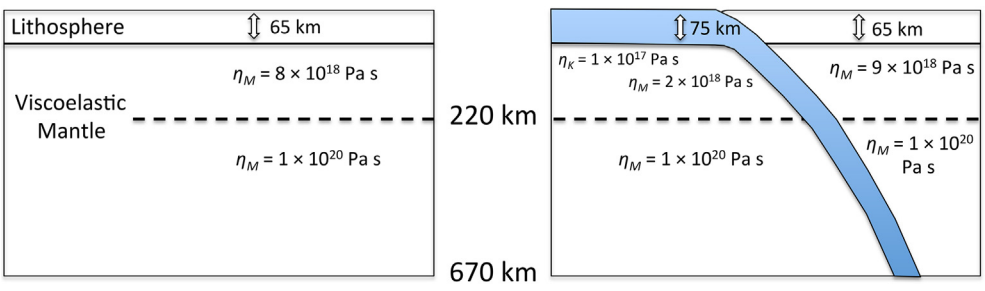

Fig. 2. Rheology models of (left) the 2004 SAE and (right) the 2012 IOE.

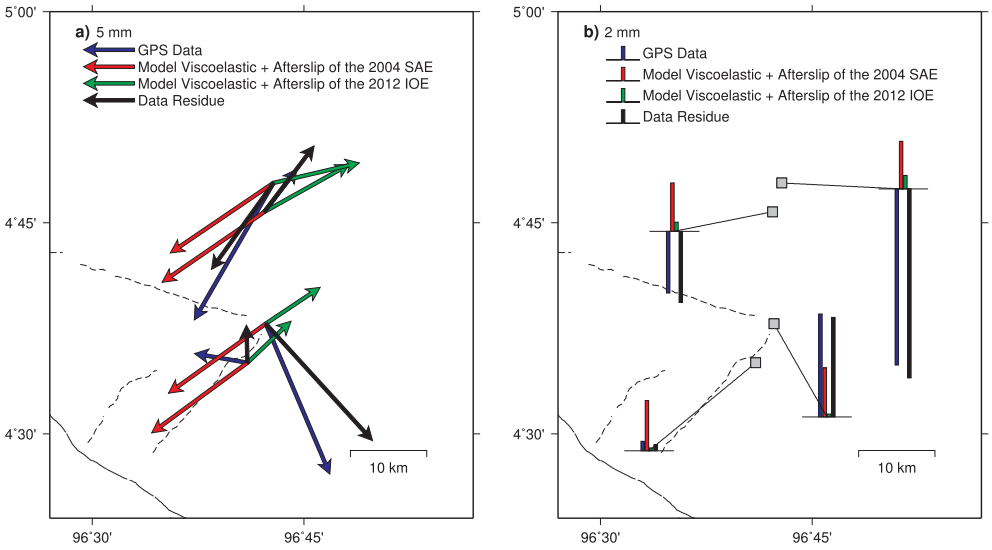

Fig. 3. Surface displacements from July to December 2013 with (a) the horizontal component and (b) the vertical component. The blue arrows/bars indicate observed data in the Sundaland reference frame, the red arrows/bars suggest the modeled postseismic deformation of the 2004 SAE, the green arrows/bars imply the modeled postseismic deformation of the 2012 IOE, and the black arrows mark the GPS data residues to be used for analyzing the postseismic deformation of the 2013 AE. The black line indicates the location of the Sumatran fault and the dashed line marks the newly identified fault segments of Pantan Terong and Celala in northern Sumatra. (For interpretation of the references to color in this figure legend, the reader is referred to the web version of this article.)

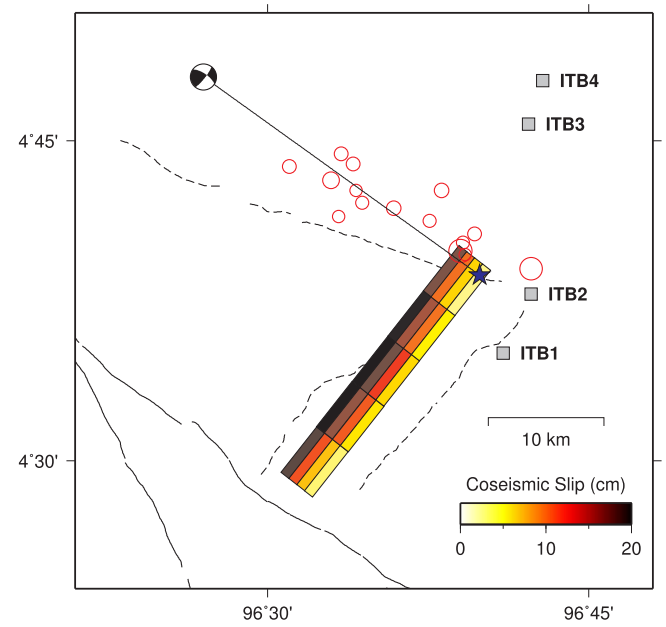

Fig. 4. Coseismic slip distribution of the 2 July 2013 AE used in our analysis from Gunawan et al. (2018). The red circles indicate the location of the four-day aftershocks. (For interpretation of the references to color in this figure legend, the reader is referred to the web version of this article.)

data suggest uplift and uplift where data suggest subsidence.

5.2. Viscoelastic relaxation

To investigate if our data set contains a signal of the viscoelastic relaxation of the 2 July 2013 AE, we construct a rheological structure with an elastic layer thickness of 65 km and a Maxwell viscosity of 8.0×10^{18} Pa·s. This rheology model follows the rheology model used in the analysis of the 2004 SAE (Gunawan et al., 2014). Viscoelastic relaxation is then calculated using VISCO1D code (Pollitz, 1997), with the coseismic slip distribution of the 2013 AE of Gunawan et al. (2018). Our results suggest that the modeled horizontal and vertical displacements are insignificant (< 0.005 mm). Moreover, model displacement suggests subsidence at all GPS stations. Fig. 6 shows the displacement model compared with data for the horizontal and vertical components.

5.3. Afterslip

The different directions and magnitudes of displacements suggest that afterslip most likely occurred at multiple fault segments. While displacements at ITB 1 and ITB 2 are affected by the deformation of the Pantan Terong segment, displacements at ITB 3 and ITB 4 are affected by the deformation of the Celala segment.

We estimate afterslip by inverting the GPS data for a dislocation model in the elastic half-space (Okada, 1992). Here, we search for only rake and slip. We run a couple of models to find the best-fit estimation of the data and model. We first construct two fault patches along the left-lateral Celala segment, extended from the coseismic fault plane in the northeast direction. The fault size is 20 km × 10 km, with a top depth of 1 km and 10 km. The fault strike is 38° in the north clockwise direction, dipping 80° in the south direction. Using this model, estimated displacement poorly matches data at the GPS stations with $\chi^2 = 7$ mm, where $\chi^2 = (\sum_{i=1,n} (data_i - model_i)^2)/n$.

We then add a fault model along the right-lateral fault Pantan Terong segment with a size of 30 km × 10 km and a top depth of 1 km. The fault strike is 290° in the north clockwise direction, dipping 69° in the east direction. Instead of getting better, misfit worsens with χ^2=15 mm. We then add a deeper fault patch at this segment, so that the Pantan Terong segment has two fault patches. We find that model displacement better fits the data with $\chi^2 = 2$ mm. We then shorten the length of the deeper fault patch of the Pantan Terong segment and find that $\chi^2 = 3$ mm, slightly worse than in the previous model. Fig. 7 shows our best estimate of the afterslip inversion result.

6. Discussion

The 2013 M_w 6.1 AE occurred almost a decade after the occurrence of the 2004 M_w 9.2 SAE. Considering that the 2004 SAE was a magnitude 9-class earthquake, it is no surprise that postseismic deformation may still continue many years ahead. Take this example of another magnitude 9–class earthquake, namely the 1960 M_w 9.2 Alaska earthquake. Geodetic data from 1965 to 2007 indicated an ongoing postseismic deformation process associated with viscoelastic relaxation and afterslip (Suito and Freymueller, 2009). Similarly, it is well understood that the postseismic deformation of the 2012 M_w 8.6 IOE affected the near-field region, especially in northern Sumatra (Han et al., 2015; Hu et al., 2016; Pratama et al., 2017). It is interesting to note that although the time passed after the 2004 SAE is longer than the 2012 IOE, the postseismic displacement model is still larger at 50–80%.

Our results for poroelastic rebound after the 2013 M_w 6.1 AE suggest

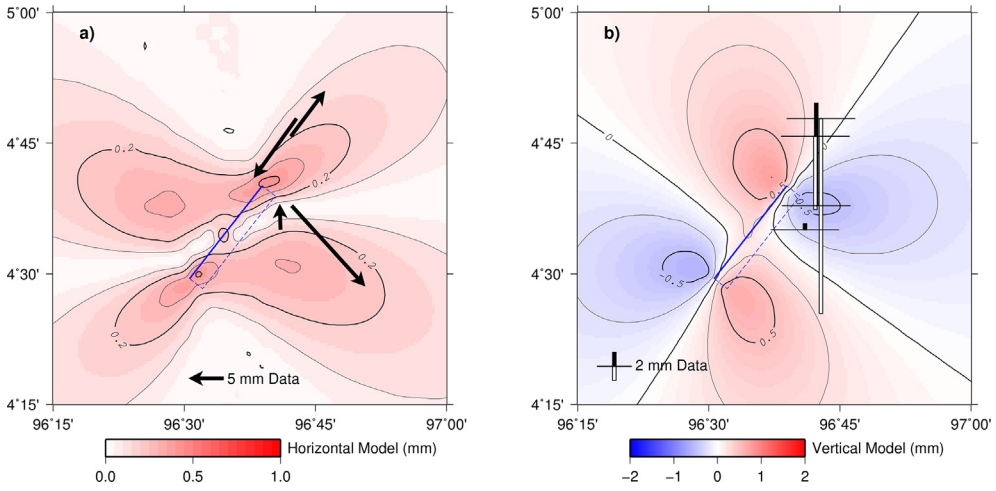

Fig. 5. Modeled poroelastic rebound displacements for (a) horizontal and (b) vertical. The black bars indicate uplift while the white bars denote subsidence. The blue line denotes the surface projection of the coseismic fault model used in this study. The solid black line indicates the displacement model contour in millimeters. (For interpretation of the references to color in this figure legend, the reader is referred to the web version of this article.)

that the displacement results have a low magnitude in the horizontal component and inconsistencies in the vertical component between the model and data. With such characteristics, we omit the poroelastic rebound responsible for the 2013 AE. Although poroelastic rebound may have occurred after the main shock, unfortunately signals have disappeared from our currently available data. Most likely, even if the process occurred, it was completed within a matter of days, not months, as on the scale of our currently available data set. Similarly, the very small and insignificant viscoelastic displacement model clearly suggests that the 2013 M_w 6.1 AE did not drive viscoelastic flow in the mantle.

By ruling out contributions from poroelastic rebound and viscoelastic relaxation, the only candidate attributed to the data displacement is afterslip. Our afterslip moment estimation over July to December 2013 is 8.51×10^{18} N·m (equivalent to M_w 6.5), using a value of 30 GPa for rigidity. This finding suggests that afterslip during July to December 2013 generated a moment release ~4 times higher than the coseismic rupture (1.97×10^{18} N·m, equivalent to a magnitude of M_w 6.1).

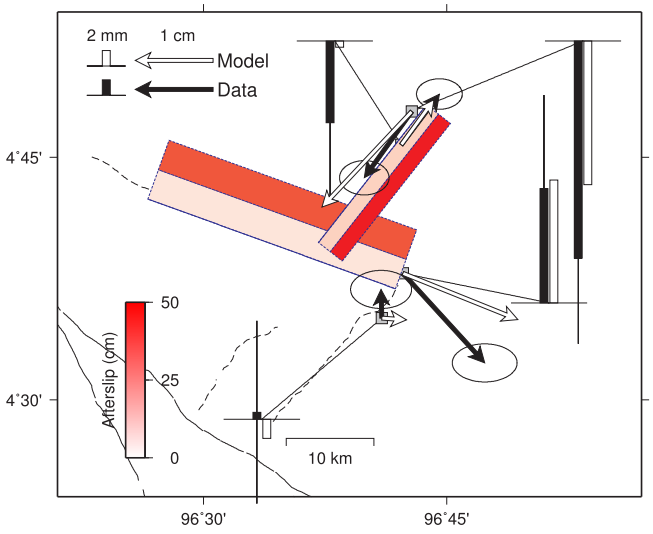

Fig. 7. Afterslip inversion result. The solid blue lines indicate the surface projection of the afterslip fault model used in the inversion. The black arrows/bars denote the data residues, while the white arrows/bars imply the afterslip displacement model. (For interpretation of the references to color in this figure legend, the reader is referred to the web version of this article.)

7. Conclusion

We analyzed GPS data displacements after the 2 July 2013 M_w 6.1 AE, and found that during July to December 2013:

- The postseismic deformation of the 2004 M_w 9.2 SAE and the 2012 M_w 8.6 IOE still affected northern Sumatra by ~12 mm and ~10 mm, respectively.
- The 2013 M_w 6.1 AE did not drive poroelastic rebound and viscoelastic relaxation.
- Afterslip occurred along two different fault segments of Celala and

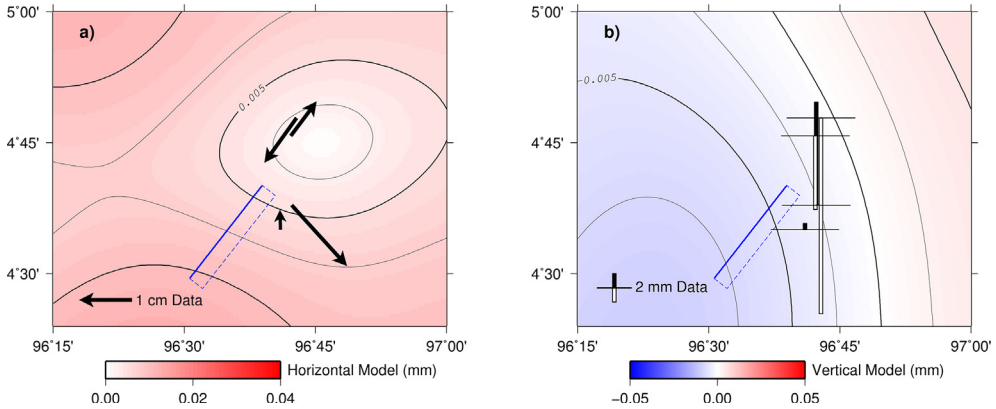

Fig. 6. Modeled viscoelastic relaxation displacements for (a) horizontal and (b) vertical. The black bars indicate uplift while the white bars denote subsidence. The blue line denotes the surface projection of the coseismic fault model used in this study. The solid black line indicates the displacement model contour in millimeters. (For interpretation of the references to color in this figure legend, the reader is referred to the web version of this article.)

Pantan Terong, with the afterslip moment during those time periods ~4 times higher than the coseismic moment.

Conflict of interest

The authors declared that there is no conflict of interest.

Acknowledgements

We thank the Editor-in Chief Mei-Fu Zhou and anonymous referees for the critical reviews. We are grateful to students from Bandung Institute of Technology who participated in GPS surveys. This study was partially supported by the 2018 World Class University Research Fund of Bandung Institute of Technology for National Postdoctoral Researcher. Figures were generated using GMT software (Wessel and Smith, 1998).

Appendix A. Supplementary material

Supplementary data to this article can be found online at https://doi.org/10.1016/j.jseaes.2019.03.020.

References

Aagaard, B.T., Knepley, M.G., Williams, C.A., 2013. A domain decomposition approach to implementing fault slip in finite-element models of quasi-static and dynamic crustal deformation. J. Geophys. Res. Solid Earth 118 (6), 3059–3079.

Aagaard, B.T., Kientz, S., Knepley, M.G., Strand, L., Williams, C.A., 2015. PyLith User Manual, Version 2.1.0. Computational Infrastructure of Geodynamic, Davis, CA. geodynamics.org/cig/software/pylith/pylith_manual-2.1.0.pdf.

Altamimi, Z., Collilieux, X., Métivier, L., 2011. ITRF2008: an improved solution of the international terrestrial reference frame. J. Geod. 85 (8), 457–473.

Delescluse, M., Chamot-Rooke, N., Cattin, R., Fleitout, L., Trubienko, O., Vigny, C., 2012. April 2012 intra-oceanic seismicity off Sumatra boosted by the Banda-Aceh mega-thrust. Nature 490 (7419), 240.

Dach, R., Lutz, S., Walser, P., Fridez, P. (Eds.), 2015. Bernese GNSS Software Version 5.2, User manual. Astronomical Institute, University of Bern, Bern Open Publishing. https://doi.org/10.7892/boris.72297.

Feng, L., Hill, E.M., Banerjee, P., Hermawan, I., Tsang, L.L., Natawidjaja, D.H., Suwargadi, B.W., Sieh, K., 2015. A unified GPS-based earthquake catalog for the Sumatran plate boundary between 2002 and 2013. J. Geophys. Res. Solid Earth 120 (5), 3566–3598.

Freed, A.M., 2007. Afterslip (and only afterslip) following the 2004 Parkfield, California, earthquake. Geophys. Res. Lett. 34 (6).

Gunawan, E., Sagiya, T., Ito, T., Kimata, F., Tabei, T., Ohta, Y., Meilano, I., Abidin, H.Z., Agustan, Nurdin, I., Sugiyanto, D., 2014. A comprehensive model of postseismic deformation of the 2004 Sumatra-Andaman earthquake deduced from GPS observations in northern Sumatra. J. Asian Earth Sci. 88, 218–229. https://doi.org/10.1016/j.jseaes.2014.03.016.

Gunawan, E., Meilano, I., Abidin, H.Z., Hanifa, N.R., Susilo, 2016a. Investigation of the best coseismic fault model of the 2006 Java tsunami earthquake based on mechanisms of postseismic deformation. J. Asian Earth Sci. 117, 64–72. https://doi.org/10.1016/j.jseaes.2015.12.003.

Gunawan, E., Maulida, P., Meilano, I., Irsyam, M., Efendi, J., 2016b. Analysis of coseismic fault slip models of the 2012 Indian Ocean earthquake: importance of GPS data for crustal deformation studies. Acta Geophys. 64 (6), 2136–2150. https://doi.org/10.1515/acgeo-2016-0106.

Gunawan, E., Widiyantoro, S., Rosalia, S., Daryono, M.R., Meilano, I., Supendi, P., Ito, T., Tabei, T., Kimata, F., Ohta, Y., Ismail, N., 2018. Coseismic slip distribution of the 2 July 2013 Mw 6.1 Aceh, Indonesia, earthquake and its tectonic implications. Bull. Seismol. Soc. Am. https://doi.org/10.1785/0120180035.

Han, S.C., Sauber, J., Pollitz, F., 2015. Coseismic compression/dilatation and viscoelastic uplift/subsidence following the 2012 Indian Ocean earthquakes quantified from satellite gravity observations. Geophys. Res. Lett. 42 (10), 3764–3772.

Hill, E.M., Yue, H., Barbot, S., Lay, T., Tapponnier, P., Hermawan, I., Hubbard, J., Banerjee, P., Feng, L., Natawidjaja, D., Sieh, K., 2015. The 2012 Mw 8.6 Wharton basin sequence: a cascade of great earthquakes generated by near-orthogonal, young, oceanic mantle faults. J. Geophys. Res. Solid Earth 120 (5), 3723–3747.

Hu, Y., Bürgmann, R., Banerjee, P., Feng, L., Hill, E.M., Ito, T., Tabei, T., Wang, K., 2016. Asthenosphere rheology inferred from observations of the 2012 Indian Ocean earthquake. Nature 538 (7625), 368.

Indonesian National Board for Disaster Management (BNPB), 2013. Earthquake hit Aceh. Majalah Gema BNPB 4 (2), 38–44.

Ito, T., Gunawan, E., Kimata, F., Tabei, T., Simons, M., Meilano, I., Agustan, Ohta, Y., Nurdin, I., Sugiyanto, D., 2012. Isolating along-strike variations in the depth extent of shallow creep and fault locking on the northern Great Sumatran Fault. J. Geophys. Res. Solid Earth (1978–2012) 177 (B6).

Ito, T., Gunawan, E., Kimata, F., Tabei, T., Meilano, I., Agustan, Ohta, Y., Ismail, N., Nurdin, I., Sugiyanto, D., 2016. Co-seismic offsets due to two earthquakes (Mw 6.1) along the Sumatran fault system derived from GNSS measurements. Earth Planets Space 68 (1), 1. https://doi.org/10.1186/s40623-016-0427-z.

Jarvis, A., Reuter, H.I., Nelson, A., Guevara, E., 2008. Hole-Filled SRTM for the Globe Version 4. Available from the CGIAR-CSI SRTM 90m Database (http://srtm.csi.cgiar.Org).

Jónsson, S., Segall, P., Pedersen, R., Björnsson, G., 2003. Post-earthquake ground movements correlated to pore-pressure transients. Nature 424 (6945), 179–183.

Lorenzo-Martín, F., Roth, F., Wang, R., 2006. Inversion for rheological parameters from post-seismic surface deformation associated with the 1960 Valdivia earthquake, Chile. Geophys. J. Int. 164 (1), 75–87.

Lyard, F., Lefevre, F., Letellier, T., Francis, O., 2006. Modelling the global ocean tides: modern insights from FES2004. Ocean Dyn. 56 (5–6), 394–415.

Miyazaki, S.I., Segall, P., Fukuda, J., Kato, T., 2004. Space time distribution of afterslip following the 2003 Tokachi-oki earthquake: implications for variations in fault zone frictional properties. Geophys. Res. Lett. 31 (6).

Okada, Y., 1992. Internal deformation due to shear and tensile faults in a half-space. Bull. Seismol. Soc. Am. 82 (2), 1018–1040.

Peltzer, G., Rosen, P., Rogez, F., Hudnut, K., 1998. Poroelastic rebound along the Landers 1992 earthquake surface rupture. J. Geophys. Res. Solid Earth (1978–2012) 103 (B12), 30131–30145.

Pollitz, F.F., 1997. Gravitational viscoelastic postseismic relaxation on a layered spherical Earth. J. Geophys. Res. Solid Earth 102 (B8), 17921–17941.

Pollitz, F.F., Bürgmann, R., Thatcher, W., 2012. Illumination of rheological mantle heterogeneity by the M7. 2 2010 El Mayor-Cucapah earthquake. Geochem. Geophys. Geosyst. 13 (6).

Pratama, C., Ito, T., Sasajima, R., Tabei, T., Kimata, F., Gunawan, E., Ohta, Y., Yamashina, T., Ismail, N., Nurdin, I., Sugiyanto, D., 2017. Transient rheology of the oceanic asthenosphere following the 2012 Indian Ocean Earthquake inferred from geodetic data. J. Asian Earth Sci. 147, 50–59. https://doi.org/10.1016/j.jseaes.2017.07.049.

Rhie, J., Dreger, D., Bürgmann, R., Romanowicz, B., 2007. Slip of the 2004 Sumatra–Andaman earthquake from joint inversion of long-period global seismic waveforms and GPS static offsets. Bull. Seismol. Soc. Am. 97 (1A), S115–S127.

Sieh, K., Natawidjaja, D., 2000. Neotectonics of the Sumatran fault, Indonesia. J. Geophys. Res. Solid Earth 105 (B12), 28295–28326.

Simons, W.J.F., Socquet, A., Vigny, C., Ambrosius, B.A.C., Haji Abu, S., Promthong, C., Subarya, C., Sarsito, D.A., Matheussen, S., Morgan, P., Spakman, W., 2007. A decade of GPS in Southeast Asia: resolving Sundaland motion and boundaries. J. Geophys. Res. Solid Earth 112 (B6).

Suito, H., Freymueller, J.T., 2009. A viscoelastic and afterslip postseismic deformation model for the 1964 Alaska earthquake. J. Geophys. Res. Solid Earth 114 (B11).

van Dam, T. and Ray, R., 2010. Updated October 2010. S1 and S2 Atmospheric Tide Loading Effects for Geodetic Applications. At < http://geophy.uni.lu/ggfc-atmosphere/tide-loading-calculator.html > (Data set/Model accessed YYYY-MM-DD).

Wang, K., Hu, Y., He, J., 2012. Deformation cycles of subduction earthquakes in a viscoelastic Earth. Nature 484 (7394), 327–332.

Wessel, P., Smith, W.H., 1998. New, improved version of Generic Mapping Tools released. Eos, Trans. Am. Geophys. Union 79 (47), 579.

Wiseman, K., Bürgmann, R., 2012. Stress triggering of the great Indian Ocean strike-slip earthquakes in a diffuse plate boundary zone. Geophys. Res. Lett. 39 (22).

Yadav, R.K., Kundu, B., Gahalaut, K., Catherine, J., Gahalaut, V.K., Ambikapthy, A., Naidu, M.S., 2013. Coseismic offsets due to the 11 April 2012 Indian Ocean earthquakes (Mw 8.6 and 8.2) derived from GPS measurements. Geophys. Res. Lett. 40 (13), 3389–3393.